DLP 3D Printing of LevoglucosenoneBased Monomers: Exploiting Thiolene Chemistry for BioBased Polymeric Resins

ChemSusChem

Research Article
doi.org/10.1002/cssc.202301828

Chemistry Europe
European Chemical Societies Publishing

www.chemsuschem.org

DLP 3D Printing of Levoglucosenone-Based Monomers: Exploiting Thiol-ene Chemistry for Bio-Based Polymeric Resins

Lorenzo Pezzana,[a] Sami Fadlallah,*[b] German Giri,[b] Corentin Archimbaud,[b] Ignazio Roppolo,[a] Florent Allais,*[b] and Marco Sangermano[a]

Additive manufacturing (AM) is a well-established technique that allows for the development of complex geometries and structures with multiple applications. While considered a more environmentally-friendly method than traditional manufacturing, a significant challenge lies in the availability and ease of synthesis of bio-based alternative resins. In our endeavor to valorize biomass, this work proposes the synthesis of new α,ω-dienes derived from cellulose-derived levoglucosenone (**LGO**). These dienes are not only straightforward to synthesize but also offer a tunable synthesis approach. Specifically, **LGO** is first converted into diol precursor, which is subsequently esterified using various carboxylic acids (in this case, 3-butenoic, and 4-pentenoic acids) through a straightforward chemical pathway. The resulting monomers were then employed in UV-activated thiol-ene chemistry for digital light process (DLP). A comprehensive study of the UV-curing process was carried out by Design of Experiment (DoE) to evaluate the influence of light intensity and photoinitiator to find the optimal curing conditions. Subsequently, a thorough thermo-mechanical characterization highlighted the influence of the chemical structure on material properties. 3D printing was performed, enabling the fabrication of complex and self-stain structures with remarkable accuracy and precision. Lastly, a chemical degradation study revealed the potential for end-of-use recycling of the bio-based thermosets.

Introduction

Sustainability and green development are paramount in today's research, with a pressing need to reduce reliance on fossil-based materials and mitigate green-house gas emissions.[1–3] Different strategies are being explored to achieve these goals, one of which involves harnessing of bio-based monomers to produce green materials.[4] Among the primary sources of these chemicals, cellulose, lignocellulose, and lignin stand out as key components that can be converted into a variety of chemicals for diverse applications.[5] The worldwide availability of the raw materials, the low cost, the possibility to use side streams of industry, such as pulp and paper,[6–8] and the profuse chemical versatility make them interesting and useful candidates to generate new bio-derived materials.[9–11] Indeed, the use of renewable and abundant plant resources, rich in cellulose, offers a promising solution.[12] Biomass pyrolysis, a key biorefinery technology, facilitates the conversion of biomass into solid, liquid and gaseous products, nevertheless, the complexities and costs associated with biomass pyrolysis have led to the development of selective pyrolysis techniques.[13] This is the case with levoglucosenone (**LGO**), a valuable building block derived from cellulosic waste by flash pyrolysis.[14] The remarkable reactivity of **LGO**, with its α,β-unsaturated ketone structure, paves the way for efficient structural modifications and the creation of easily polymerizable monomers.[15] This versatility enabled the synthesis of a variety of **LGO**-based polymers, including polycyclic olefins,[16] polyesters,[17,18] polycarbonates,[19,20] and poly(vinyl ether lactone).[21] For example, a green and efficient two-step, one-pot process has recently been developed for the conversion of **LGO** to (1R,2S,5R)-6,8-dioxabicyclo[3.2.1]octane-2,4-diol (**HO-LGOL**), using K_3PO_4 as the base catalyst (Scheme 1). This led to the synthesis of polyesters by subsequent condensation of **HO-LGOL** with aliphatic comonomers (diacyl chloride and diesters). However, it is important to recognize certain limitations of these polycondensation techniques. Firstly, they suffer from a lack of precise control of

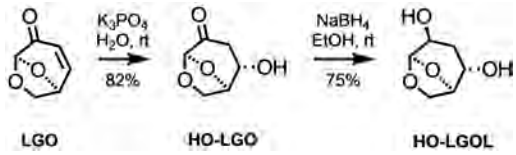

Scheme 1. Synthesis of **HO-LGOL** from **LGO**.

[a] *Dipartimento Scienza e Tecnologia dei Materiali (DISAT), Politecnico di Torino, Torino, Italy*
[b] *URD Agro-Biotechnologies Industrielles (ABI), AgroParisTech, Pomacle, France*

***Correspondence:** Sami Fadlallah and Florent Allais, URD Agro-Biotechnologies Industrielles (ABI), AgroParisTech, 3 rue des Rouges Terres, 51110 Pomacle, France.*
Email: sami.fadlallah@agroparistech.fr and florent.allais@agroparistech.fr

Supporting Information for this article is available on the WWW under https://doi.org/10.1002/cssc.202301828

the polymerization process, in addition, unwanted side reactions occurred during polymerization due to the use of harsh conditions, resulting in reduced yields and very low molecular weights.

While the use of bio-based monomers is a step in the right direction, alone it cannot fully address sustainability and green development concerns. Indeed, a synergistic approach involving eco-friendly processes is essential.[22] As a result, there has been a growing interest in UV-curing technology, which not only offers advantages such as reduced energy consumption, shorter production time, and cost-effectiveness,[23,24] but also enables additive manufacturing (AM) applications, spanning a diverse array of industries, ranging from electronics to aerospace.[25,26]

AM relies on the rapid curing of UV-reactive functional groups, allowing a layer-by-layer printing to create intricate and self-stain structures.[27] Two crucial features of the polymeric resins used in AM are fast reactivity to reduce printing time and suitable viscosity to create a uniform layer on the 3D printer's VAT. Recent research has explored the use of not only fossil-based resins but also bio-based resins.[28–30] However, to exploit photocuring process, specific chemical groups are required to promote chain-growth or step-growth curing mechanism. Among the multiple possibilities, which include epoxy monomers for cationic UV-curing,[31] and acrylate, methacrylate monomers for radical curing,[32,33] the allyl monomers have gained attention for their compatibility with thiol-ene chemistry.[34–37]

Thiol-ene click chemistry is an appealing process characterized by its high conversion rates owing to its "click" feature, involving a stereospecific and orthogonal 1:1 reaction between thiol and ene functionalities.[38,39] An additional benefit is the absence of oxygen inhibition which addresses production-related challenges. In essence, this chemistry tends to align with green chemistry principles, as it typically requires mild reaction conditions, produces minimal hazardous by-products, and often utilizes less energy. Thiol-ene reaction has been investigated with various bio-based platforms in recent years, including terpenes,[34,40,41] furans,,[36,42] isosorbide[37,43,44] and levoglucosan derivatives.[45–47]

In our previous work,[47] **LGO** was investigated as a platform molecule to develop allyl-containing monomers for thiol-ene chemistry expendable also in AM. These monomers, synthesized from LGO via a series of reactions including oxa-Michael addition, Baeyer-Villiger oxidation, and enzymatic transesterification with diesters, influenced the thermo-mechanical properties of the resulting thermosets, offering a range of glass transition temperatures (T_g) from −4 to 18 °C. Building on this foundation, our current study aims to further harness LGO's potential by developing a new set of monomers for UV-curing, particularly focusing on Digital Light Processing (DLP) 3D printing in AM. This initiative uses the diol molecule **HO-LGOL** to propose novel α,ω-dienes that are easily functionalized and synthesized. Although we focus on functionalizing **HO-LGOL** with 3-butenoic and 4-pentenoic acids, this method shows promise for generating a diverse array of UV-curing monomers from **LGO** (Figure 1). Our comprehensive study includes detailed UV-curing process analysis using photo-DSC, photo-rheology and FTIR analysis. Moreover, a Design of experiment (DoE) approach was employed on the UV-curing process to find

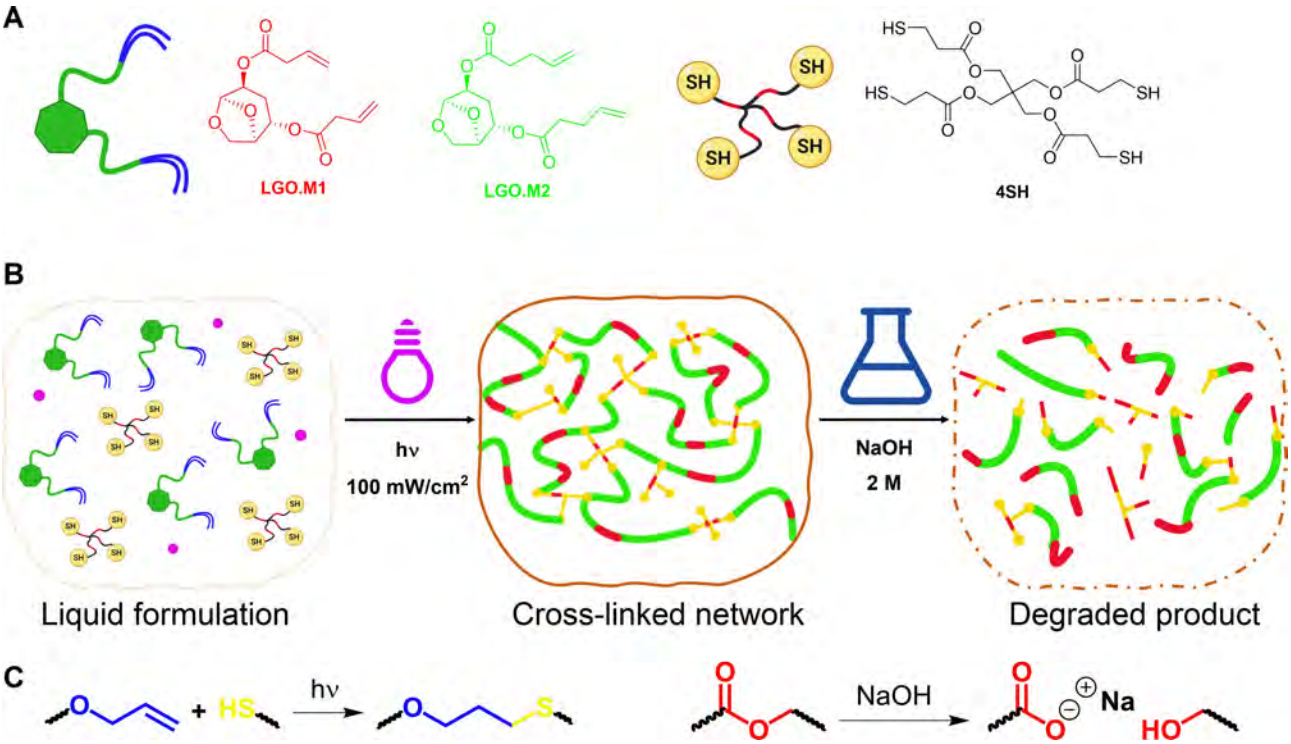

Figure 1. (A) Monomers used for the thiol-ene formulations; (B) Schematic view of the UV-curing stage and the chemical degradation step; (C) Chemical reactions involved in the UV-curing (formation of thioether linkage) and in the degradation (hydrolysis of ester bond).

the optimal condition to ensure the best conversion rates and kinetics. A thorough thermo-mechanical analysis was performed to correlate the chemical structures of the monomers with their materials properties. 3D printing was assessed through DLP to verify the feasibility of using bio-based resins in AM. Lastly, we evaluated the degradability of these thermoset materials in an alkaline environment.

Results and Discussion

Monomer Synthesis

The synthesis of the monomers **LGO-(*O*-But)$_2$** (**LGO.M1**) and **LGO-(*O*-Pent)$_2$** (**LGO.M2**) began with the stereoselective base-catalyzed Michael addition of water onto **LGO**, yielding the diastereopure alcohol **HO-LGO** (82% yield). The ketone functionality of **HO-LGO** was then reduced using sodium borohydride in ethanol to form **HO-LGOL** (75% yield) which served as a key starting material for the subsequent synthetic steps. **HO-LGOL** then underwent a Steglich esterification with two different terminal olefin-bearing carboxylic acids (i.e., 3-butenoic acid and 4-pentanoic acid) (Scheme 2). Both monomers, **LGO.M1** and **LGO.M2**, were successfully synthesized within a one-hour reaction time, yielding 83% and 93%, respectively. The validation of the structure of the products was provided by NMR analysis. Indeed, the characteristic resonances of the internal olefinic protons appear at approximately 5.8 ppm and those from the terminal protons at around 5.0 ppm for all monomers (Figure S1–S3). The ^{13}C signals of the carbons of the terminal olefin are also observed at 140 ppm and 115 ppm. Additionally, the ^{13}C NMR spectra exhibited signals at 171 ppm and 172 ppm, for ester groups of **LGO.M1** and **LGO.M2**, respectively, further confirming the successful formation of the α,ω-dienes (Figure S2 and S3).

The Steglich method was chosen for its mild conditions and avoidance of mineral acids, which could lead to unwanted side reactions with the acetal moiety in the starting material. However, it is noteworthy to mention that the Steglich reaction also has drawbacks such as the use of hazardous solvents and reagents, and the production of stoichiometric amounts of isourea to dispose of. To overcome these limitations, one can envisage the lipase-catalyzed (trans)esterification of **HO-LGOL** with the acids or the corresponding esters. Preliminary experiments with 9-decenoic and 10-undecenoic acids showed promising results. In these experiments, the diol **HO-LGOL** was reacted with the carboxylic acids at 80 °C and 25 mbar in the presence of *Candida antarctica* lipase B (CAL-B, 10% w/w). Figure S4 and S5 show the ^{1}H and ^{13}C NMR spectra of the resulting products. Although the yields were lower (66% and 43%, respectively) compared to the Steglich esterification, the successful formation of the corresponding products (see SI for more information) suggests that enzymatic routes can be a viable and more environmentally friendly alternative, warranting further optimization.

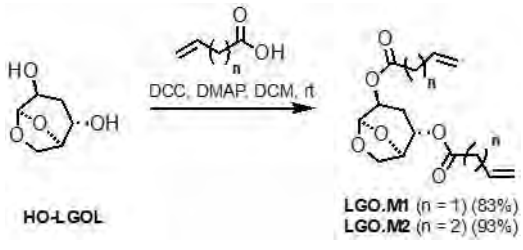

Scheme 2. Synthesis of functional α,ω-dienes **LGO-M1** and **LGO-M2** from **LGO**.

UV-Curing Process

The **LGO**-based monomers were used to develop 3D printable formulations for degradable thiol-ene networks employing a commercially available tetrafunctional thiol, as presented in Figure 1. The UV-curing process was studied by means of photo-DSC analysis employing a Design of Experiment (DoE) method to optimize the curing conditions. Indeed, the amount of photoinitiator (PhI) and the light intensity can play important roles in the UV-curing process allowing high conversion and fast kinetic.[36,48,49] The conversion can be calculated by the heat released during the UV-curing (Figure S6), knowing the theoretical heat of polymerization of a thiol-ene bond, which is around 19 kcal/mol.[50] Moreover, the h_{peak} of the thermograms can be correlated to the rate of polymerization, indeed a high h_{peak} value means a fast kinetic and high rate of polymerization.[29,30]

Thus, a DoE was performed by varying PhI's amount and UV-light intensity to have a comprehensive understanding of the UV-curing process in the range of the selected conditions. Specifically, PhI was tested in 0, 1, and 2 phr (1 phr corresponds to 1 part for 100 parts of resin, which is equivalent to approximately 0.99 % (w/w)) while the light intensity was 10, 50, and 90 mW/cm^2. Figure 2A reports the response surface obtained for the **LGO.M1_4SH**. The analysis was performed as described in Supporting Information (Figure S7 and S8 and Table S1). The model was validated with further tests done after the creation of the surface to verify the accuracy of the contour plot. As can be seen in Figure 2A, the best condition to achieve the highest conversion (around 90%) was in the region around 1.5 phr of PhI with light intensity over 30 mW/cm^2. This indication is important to achieve the best thermo-mechanical response, thus 1.5 phr was selected to conduct further analysis with **LGO.M1**.

Interestingly the **LGO.M2_4SH** behaved similarly to **LGO.M1_4SH** reaching a similar value of conversion and h_{peak} as presented in Figure 2B. Nevertheless, it is clear that **LGO.M2_4SH** was more reactive seeing the highest region of conversion shifted at lower phr of PhI (around 1 phr) with respect to the other formulation. The difference in the reactivity between the two monomers can be due to the different chemical structures of the **LGO**-based ene monomers. Indeed, the position of the C=C differs: **LGO.M1** has the "classic" allyl structure (i.e. a chain of 3-carbons with the double bond at the end) while **LGO.M2** incorporates one more CH_2 unit, increasing the spacer between the C=C double bond and the carbonyl group.

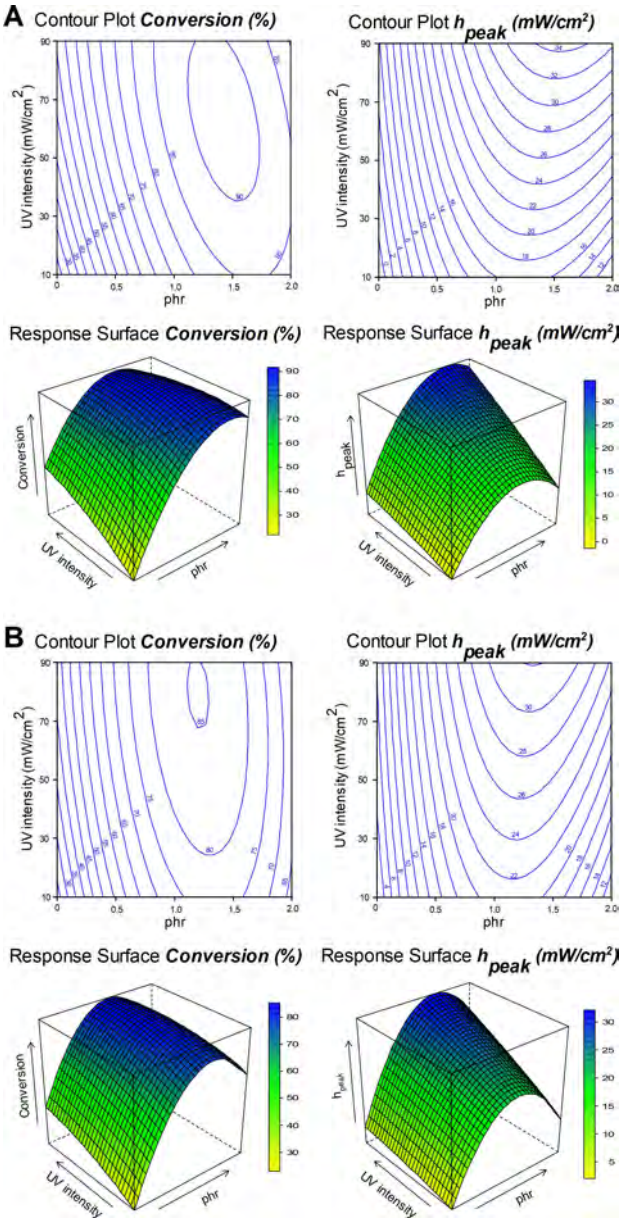

Figure 2. (A) 2D and 3D surface of the conversion and h_{peak} derived from DoE performed with photo-DSC test on **LGO.M1_4SH**; (B) response surface of **LGO.M2_4SH** formulation for conversion and h_{peak} in function of UV-intensity and phr of PhI.

The DoE allowed a comprehensive analysis of the variables that affect UV-curing, yielding valuable insights while minimizing the number of experiments required. This mapping enables a swift determination of the ideal conditions to achieve optimal conversion and rate of polymerization. For the formulations under investigation, 1.5 phr was selected as optimal condition with a light intensity over 30 mW/cm^2 to ensure a high rate of polymerization.

The difference in the reactivity was confirmed by FTIR and photorheological analysis. The FTIR analysis allowed the chemical characterization of the UV-curing process monitoring the disappearance of the thiol and ene peaks. Indeed, the thiol-ene photocurable process involved the reaction between SH and C=C double bond creating a thioether linkage.

As depicted in Figure 3, both formulations showed an almost complete disappearance of the thiol peak (2570 cm^{-1}) and ene peak (1640 cm^{-1}). The conversion was evaluated for both formulations (Equation S1), aligning with the photo-DSC values as reported in Table 1.

Additional confirmation of the "click" feature of the thiol-enereaction was provided by the real-time FTIR analysis performed with **LGO-M1_4SH**. Analyzing Figure S9 reveals a consistent conversion profile of both SH and C=C, underscoring that the reaction proceeded with a 1:1 ratio between these two functional groups.

As a last characterization stage of the UV-process, photorheology was used to examine the evolution of the storage modulus as a function of the irradiation time to assess the feasibility of printing. Indeed, a steep increase in the storage

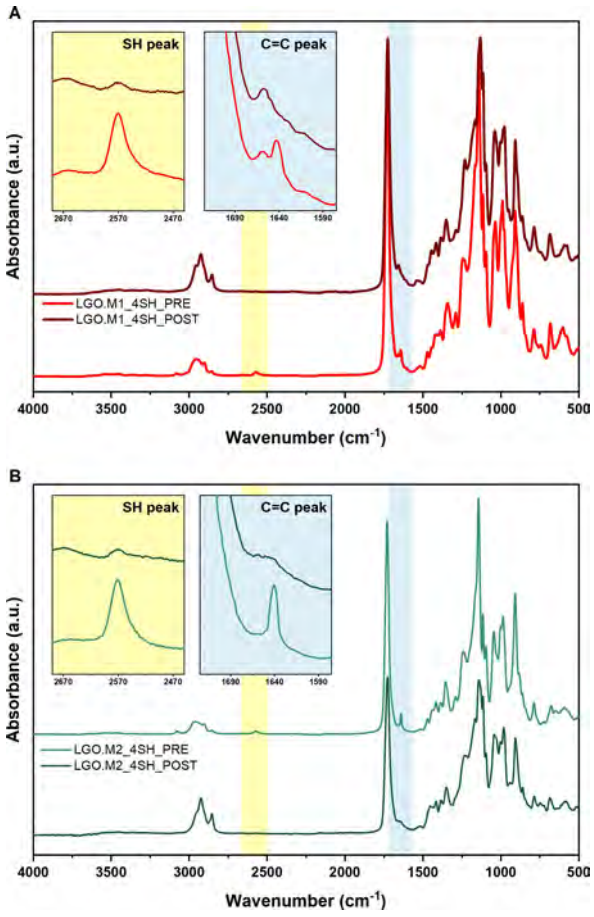

Figure 3. (A) FTIR spectra of **LGO.M1_4SH** pre and post UV-curing; (B) spectra pre and post UV-curing for the **LGO.M2_4SH**.

Table 1. UV-curing process data of photo-DSC ([1]) and FTIR ([2]) analysis.

FORMULATION	Conversion [1]	SH Conversion [2]	C=C Conversion [2]
	%	%	%
LGO.M1_4SH	90	91	92
LGO.M2_4SH	79	85	85

modulus is indicative of a fast reaction and the absence of induction time can be beneficial for the 3D printing as it reduces printing duration. Both formulations exhibited a rapid increase in the modulus as light was turned-on, signifying fast reaction as previously reported for photo-DSC results. The light intensity was varied to explore its effect on the rate of polymerization, and it is visible from Figure 4 that an increment of intensity provided a steep increase of the modulus with less induction time.

Gel content analysis confirmed the presence of an insoluble network after the UV-curing by the immersion for 24 h in chloroform. The solvent can solubilize the unreacted monomer allowing the proof of the formation of the cross-links between the monomers. **LGO.M1_4SH** achieved 88 ± 3% while **LGO.M2_4SH** reached 93 ± 3% of gel content confirming the efficacy of the thiol-ene cross-linking reaction.

Thermo-Mechanical Characterization

The thermo-mechanical performances of the bio-based UV-cured thiol-ene thermosets were evaluated by DMTA and DSC analyses. Figure 5 illustrates the DSC curves of the photocured formulations, revealing an approximately 5 °C difference between **LGO.M1_4SH** and **LGO.M2_4SH**.

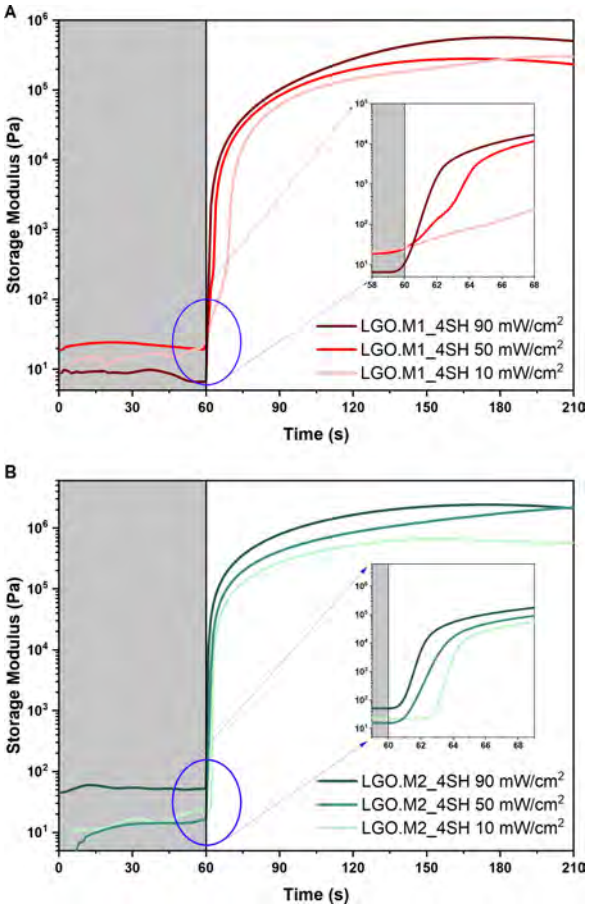

Figure 4. Storage modulus trend as a function of the time for (A) **LGO.M1_4SH** and (B) **LGO.M2_4SH** at different UV-light intensities.

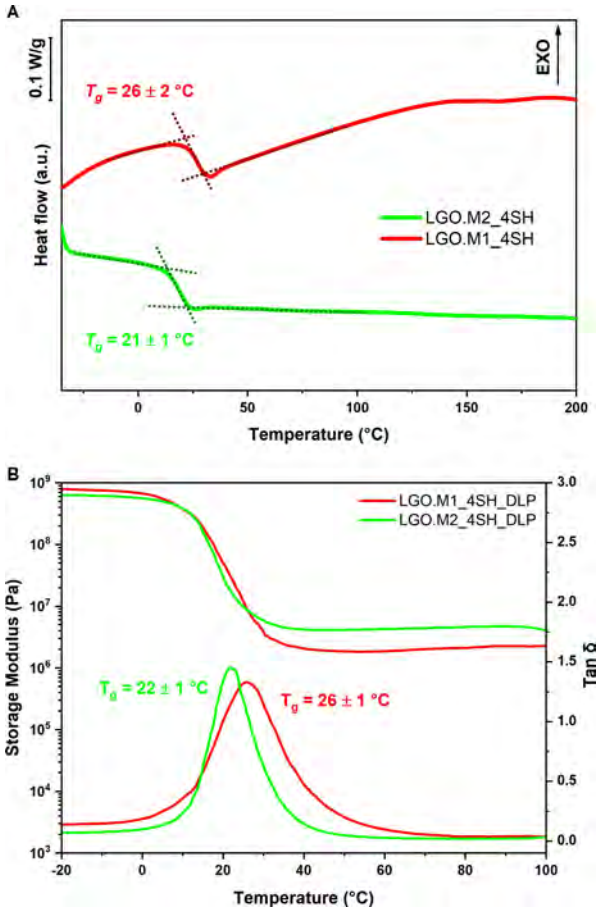

Figure 5. (A) DSC thermograms of **LGO.M1_4SH** (red) and **LGO.M2_4SH** (green); (B) Storage modulus and *Tanδ* trend in function of temperature for **LGO.M1_4SH** (red) and **LGO.M2_4SH** (green).

The slight T_g reduction observed when **LGO.M2** was used could be due to the difference in the chemical structure of the monomers. Specifically, the inclusion of an additional CH_2 unit can increase the flexibility of the network, resulting in a lower T_g compared to the network containing **LGO.M1**, which incorporates only one CH_2 unit.

The DSC results, ranging from 20 to 25 °C, were in agreement with the data recorded by DMTA analysis which reported the same T_g trend highlighting again a difference of about 5 °C between the two thermosets. The T_g of the polymers, being near room temperature, not only offers benefits such as easier processing and reduced energy consumption during printing, but also enhances its suitability for applications requiring flexibility and impact resistance (*e.g.*, soft robotics, flexible electronics, and biomedical devices).[35,37,42] The narrow shape of the *Tanδ* peak indicated quite homogeneous networks and the cross-link density was comparable for both formulations with a value of 300 and 600 mmol/dm³ for **LGO.M1_4SH** and **LGO.M2_4SH** respectively.

The mechanical properties were evaluated by tensile and compression testing (**Figure S10**). The consistency of the result was verified by the value of storage modulus reported in Table 2 where it is evident that **LGO.M1_4SH** exhibited a higher

Table 2. Mechanical properties of UV-cured samples evaluated by tensile testing (1) and compression testing (2). Elastic modulus (*Young's Modulus*), strength at break (σ), elongation (ε), toughness *(U)* and compressive modulus *(E)*.

FORMULATION	*Young's Modulus* [1]	σ [1]	ε [1]	*U* [1]	*E* [2]
	MPa	MPa	%	J/m^3 10^4	MPa
LGO.M1_4SH	12.3 ± 1.0	8.2 ± 0.6	143 ± 5	633 ± 61	37 ± 4
LGO.M_4SH	7.4 ± 1.0	5.0 ± 0.4	110 ± 9	310 ± 35	32 ± 4

value, attributed to the increased rigidity of the network. The chemical structure of **LGO.M1** may be responsible for the better properties achieved in terms of Young's modulus, strength at break, and compression's modulus.

Moreover, the higher conversion reached, as evidenced by the FTIR data, could also contribute to the enhanced performance, especially considering the highest toughness (area under the stress-strain curve) reached due to improved strength and elongation. All the data are in accordance, or even better with the previously reported ones for **LGO**-based UV-cured thiol-ene networks.[46,47]

DLP 3D Printing

The primary target of the investigation was the feasibility of using DLP as 3D printing techniques to develop complex, self-stain structures, thereby expanding the possible spectrum of applications for these **LGO**-based monomers. Firstly, the assessment started with the study of the UV-curing process which revealed fast kinetic and high conversion. Understanding the kinetics involved in 3D printing of polymer resins is essential for optimizing the process to achieve high-quality printed objects with the desired material properties.[51] However, another crucial parameters is the viscosity of the polymeric resins, which needs to be in a certain range, from 0.2 to 10 Pa×s for DLP,[52] to ensure a homogeneous distribution over the VAT, resulting in a proper layer formation. Thus, a viscosity test was performed over 24 hours to ensure the right range for the entire printing time. The time-testing was done considering the limited shelf-life of thiol-ene resins, which can react without any UV-light input leading to premature gelation.[53,54] Figure 6 reports the results for the two bio-based formulations. **LGO.M1** demonstrated greater stability, with almost no change in viscosity over 24 h, while the formulation with **LGO.M2** exhibited a shorter shelf-life, with the tendency of gelation as indicated by the increment of the viscosity after 8 hours. After 24 hours, **LGO.M2_4SH** reached a viscosity value over 10 Pa×s, rendering it unsuitable for printing. However, by carefully limiting the printing time, the 3D printing process could be successfully executed.

Overall, both formulations meet the requirements for the DLP 3D printing process which can be ensured with a careful balance between factors such as exposure time, light intensity, and velocity of the platform. Thus, to start the investigation of the 3D printing, Jacob equation (Equation 1) was used to describe the UV-curing process in a DLP system. The model

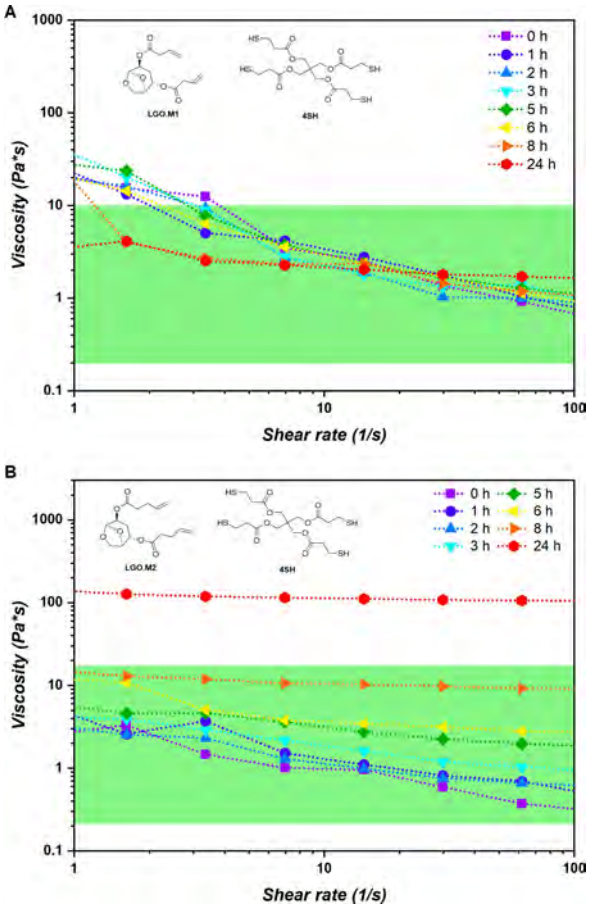

Figure 6. Viscosity over time (24 h) in function of the shear rate for **LGO.M1_4SH** (A) and **LGO.M2_4SH** (B).

generated by this Jacob equation based on the Lambert-Beer law can describe the working curves which provide crucial parameter for understanding the UV-curing.[52,55]

$$C_d = D_P \ln\left(\frac{E}{E_c}\right) \quad (1)$$

Where C_d is the curing depth at given exposure E, D_p is the penetration depth of the resin, and E_C is the critical exposure to have gelation.

Figure 7 shows the results in semi logarithmic scale to produce the so-called Jacobs working curves. The slope of the curves determines the D_P while the x-axis intercept revealed the E_C as listed in Table 3. The **LGO.M2**-based formulation had a lower E_C meaning a faster reaction as previously demonstrated by the steeper increase of the storage modulus in photo-

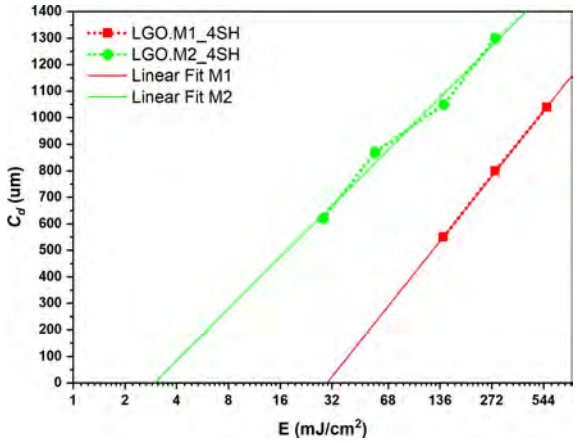

Figure 7. Jacob's curve obtained for **LGO.M1_4SH** (red) and **LGO.M1_4SH** (green).

Table 3. Curing depth (C_d), Critical exposure energy (E_C) and printing parameters used for the DLP.

FORMULATION	C_d	E_C	*Layer thickness*	*Exposure time*
	um	mJ/cm^2	um	s
LGO.M1_4SH	353	30	100	5.0
LGO.M2_4SH	281	3	100	0.5

rheology analysis (Figure 4) and by the short shelf-life. Considering the curing depth, **LGO.M1_4SH** revealed the higher value probably due to different colors and viscosities of the resins and therefore a different absorption at the printing wavelength. This test allowed to customize the printing parameters, such as exposure time, based on the specific **LGO**-based resins employed, thus optimizing the accuracy and printability of the bio-based resin.

After the setting of the printing parameters, the xy resolution was evaluated by a wall thickness evaluation comparing the 3D printed object with the original CAD file. The results, reported in Figure 8, highlighted the accuracy of both formulations with a small deviation for **LGO.M2_4SH** at low dimensions which could be caused by the high reactivity of the resin. This can create regions of over polymerization that can affect the final dimension of the object. In a complete and proper formulation for 3D printing, inhibitors or dye could be used to overcome this problem increasing accuracy of the printing. However, for this study the feasibility of AM with the bio-based resins was the main objective of the investigation. Thus, further structures were printed to prove the possibility to produce complex geometries with these resins.

The analysis of the final accuracy of the 3D printing was performed in a complete way for complex structure by 3D scanner analysis. A heatmap between CAD file and DLP printed object is created, highlighting differences. Figure 9 reports the schematic view of the different steps required for the analysis of a square pyramid 3D printed with **LGO.M2_4SH**. The green regions of the overlay map had a deviation below 100 μm with respect to the CAD file demonstrating a very high accuracy of the printing. Indeed, it is evident that the resins are suitable for fabricating complex shapes, precise and specific details containing also hollow parts.

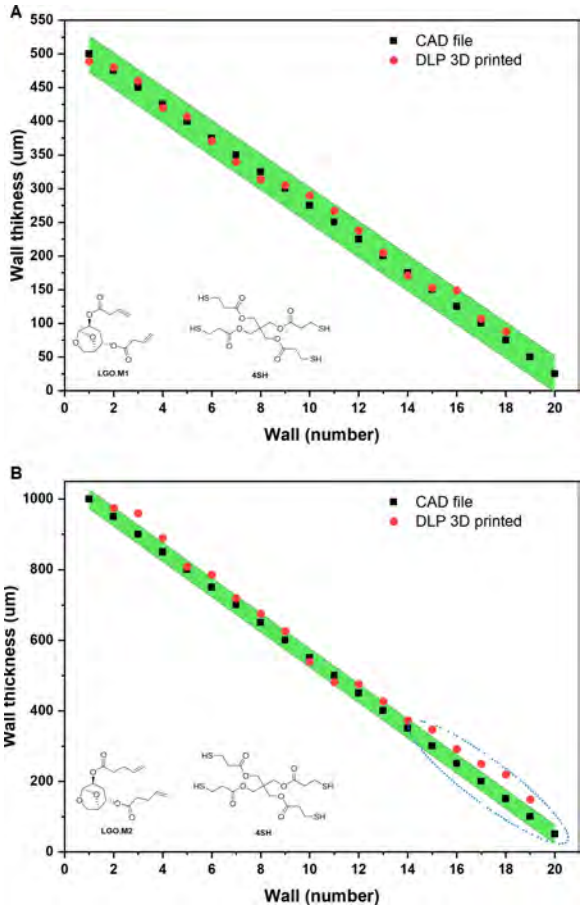

Figure 8. Resolution over xy-axis testing for **LGO.M1_4SH** (A) and **LGO.M2_4SH** (B).

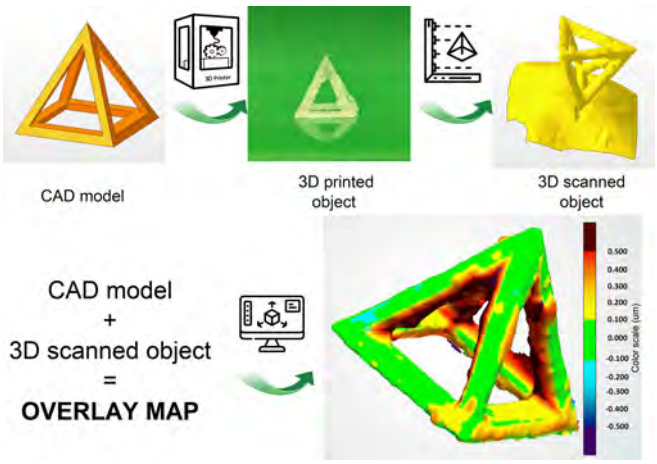

Figure 9. CAD model of square pyramid (base of 10 × 10 mm^2 and height of 10 mm), picture of 3D printed object of **LGO.M2_4SH**, 3D scanner file of the object, and overlay map with scale bar of 100 μm.

A comprehensive analysis of the 3D printed objects was carried out by printing, for both formulations, a complex ring (Figure 10), a honeycomb structure (Figure S11), and a hollow cube (Figure S12), to compare the accuracy achievable with the two resins. It is possible to affirm that both **LGO**-based formulations allowed the 3D printing of complex and self-stain structures with hollow sections. The accuracy of the resins was notably high, as visually confirmed by the extent of the green regions (representing the portion of the 3D printed part within ±100 um), as well as by the mean value, and the variance of the points detected through the 3D scanning analysis (Table 4). Overall, the **LGO.M1_4SH** shows a better outcome in terms of precision and accuracy, revealing very low mean values and variances.

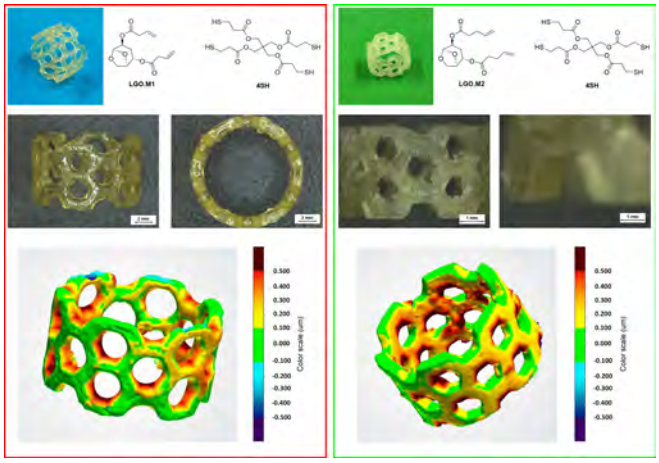

Figure 10. 3D printed object with **LGO.M1_4SH** and **LGO.M2_4SH**. The ring had a diameter of 12.56 mm and height of 7.5 mm. The scale bar unit is 100 μm.

Table 4. Data of 3D scanning analysis.

FORMULATION	*Green zone (%)*	*Mean value*	*Variance*	*Geometry*
LGO.M1_4SH	39.6	0.14	0.028	Ring (Figure 10)
LGO.M2_4SH	32.7	0.23	0.083	
LGO.M1_4SH	28.3	0.15	0.078	Honeycomb flower (Figure S11)
LGO.M2_4SH	19.7	0.23	0.116	
LGO.M1_4SH	36.2	0.21	0.070	Hollow cube (Figure S12)
LGO.M2_4SH	29.2	0.26	0.083	

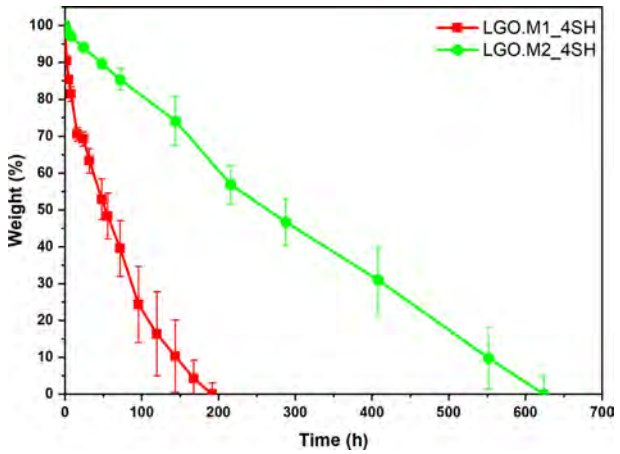

Figure 11. Degradation profile of the **LGO.M1_4SH** and **LGO.M2_4SH** in the alkaline environment.

Chemical Degradation

Considering the chemical structure of the monomers involved in the UV-cured polymer networks, a degradation study was conducted. Indeed, the ester bonds present in the backbone of the networks are susceptible to hydrolysis in alkaline environment, leading to the cleavage of the polymer chains, as previously demonstrated.[46,47] Figure 11 shows the weight loss trend of the two formulations as a result of the degradation of the networks in alkaline environment (NaOH 2 M). Interestingly, the **LGO.M1** completely degraded within 200 hours, while **LGO.M2**-based network had higher chemical stability showing a complete weight loss in 600 hours. The varying rates of degradation indicate that the shorter alkyl chain in **LGO.M1_4SH** leads to quicker hydrolysis. This outcome might stem from an easier-to-access structure within the polymer matrix, which enables more water to penetrate and accelerates the hydrolysis process. Conversely, **LGO.M2_4SH**, which possesses a longer alkyl chain, may likely form interpenetrated and more hydrophobic network chains that hinder water infiltration, resulting in a reduced rate of degradation. This finding presents a possible approach for the end-of-life management of the thermoset, improving the green aspects of the newly synthesized materials.

Conclusions

The synthesis of these new **LGO**-derived monomers represents a step forward in the development of bio-based materials for additive manufacturing, demonstrating the potential of leveraging renewable resources in creating high-performance polymeric resins. While the current synthesis route of the α,ω-dienes offers several advantages in terms of efficiency and the utilization of mild conditions, we recognize the importance of improving the sustainability of our processes. Looking ahead, one possible direction for enhancing the green chemistry aspects of our work is the exploration of enzymatic condensation reactions. Indeed, preliminary experiments using 9-decenoic and 10-undecenoic acids with **HO-LGOL** in the presence of a lipase, have demonstrated the feasibility of enzymatic reactions, though further optimization is necessary to increase the yield. These findings highlight the potential for greener synthesis pathways in future studies.

The reactivity of the developed monomers towards thiol-ene polymerization, as revealed through a thorough DoE analysis of the UV-curing process, underscores the technical feasibility of our approach. Optimal UV-curing conditions were identified, notably employing 1.5 phr of photoinitiator and light

intensity above 30 mW/cm^2. Among the **LGO**-based thermosets, those derived from **LGO.M1** exhibited the best thermo-mechanical performance achieving T_g of about 25 °C and remarkable strength of 8.2 MPa. This can be attributed to the chemical structure of this **LGO** allyl monomer which contains only one CH_2 unit. In contrast, **LGO.M2** with two CH_2 units, offers higher reactivity but lower mechanical performance. The feasibility of the 3D printing was proven by DLP which was successful for both bio-based resins. The 3D structures were deeply analyzed to verify accuracy and precision which were remarkable. Finally, the presence of ester bonds inside the polymer backbone allowed the chemical degradation of the network, presenting opportunities for recycling at the end-of-life of the products. Overall, this study underscores the potential for developing environmentally friendly resins starting from **LGO** for 3D printing applications, contributing to sustainable and eco-conscious development.

Experimental Section

Materials

Levoglucosenone (LGO) was provided by Circa. Potassium phosphate tribasic (K_3PO_4, 98%), sodium borohydride ($NaBH_4$, 98%), 4-(Dimethylamino) pyridine (DMAP, 99%), 4-pentenoic acid (95%), 9-decenoic acid (95%) were purchased from Sigma-Aldrich. *N*,*N*′-dicyclohexylcarbodiimide (DCC, 99%) was purchased from Acros Organics. 3-butenoic acid (95%) was purchased from Fisher. 10-undecenoic acid (95%) was purchased from TCI. Cyclohexane, ethyl acetate, ethanol and acetonitrile analytical norm were purchased from VWR. Dichloromethane (DCM) and tetrahydrofuran analytical norm were purchased from Fisher and Sigma-Aldrich, respectively. Nuclear magnetic resonance (NMR) solvents including $CDCl_3$ and DMSO-d_6 were purchased from Sigma and Eurisotop, respectively. The thiol monomer, pentaerythritol tetrakis(3-mercaptopropionate) (PETMP, 95%), was provided by Sigma-Aldrich. The photoinitiator, phenylbis(2,4,6- trimethylbenzoyl) phosphine oxide, Irgacure 819 (BAPO, 97%), was purchased from BASF.

Analytical Instrumentation

Chromatographic Purification. Chromatographic purification was accomplished by using a flash-prep LC system puriFlash 4100 from Interchim with prepacked silica column (30 μm, Interchim PFSi30-HP), dual-wavelength collection (λ = 254 and 320 nm).

NMR Spectroscopy. ^{1}H NMR spectra were recorded on a Bruker Fourier 300 (300 MHz) and were calibrated with a residual DMSO-d_6 signal at δ 2.50 and a $CDCl_3$ residual signal at 7.26 ppm. Data are reported as follows: chemical shift (δ ppm), multiplicity, coupling constant (Hz), integration, and assignment. ^{13}C NMR spectra were recorded on a Bruker Fourier 300 (75 MHz) and were calibrated with DMSO-d_6 at δ 39.5 and $CDCl_3$ at δ 77.2 ppm. All NMR assignments were also made using ^{1}H−^{1}H COSY, ^{1}H−^{13}C HMBC, and ^{1}H−^{13}C HSQC spectra.

Polarimetry. Optical activity was measured in a Belingham Stanley polarimeter at a compound concentration of 0.02 g/mL.

Fourier Transform IR (FTIR). The conversion of SH and C=C bonds was evaluated by attenuated total reflectance (ATR) FTIR analysis by means of Nicolet iS 50 Spectrometer. The spectra were collected with a spectral resolution of 4 cm^{-1}. All the data were handled by Onmic software developed by Thermo Fisher Scientific. The conversion values were collected by monitoring the disappearance of the thiol peaks at 2570 cm^{-1} and the carbon-carbon double bond at 1640 cm^{-1}. The peak at 1730 cm^{-1} was taken as a reference. It was assumed to be unaffected by UV-irradiation since it belonged to the C=O bending of the ester that was not involved into the curing reaction. Equation 2 was used to calculate the conversion pre and post UV-irradiation.

$$Conversion\ (\%) = \frac{\left(\frac{A_{fun}}{A_{ref}}\right)_{pre} - \left(\frac{A_{fun}}{A_{ref}}\right)_{post}}{\left(\frac{A_{fun}}{A_{ref}}\right)_{pre}} \times 100 \quad (2)$$

where A_{fun} is the area of the functional group under investigation (e.g. area of the thiol at 2570 cm^{-1}) while A_{ref} is the area of the peak at 1730 cm^{-1}. The area was normalized to give the conversion and then an average of three measures was taken.

Furthermore, a real-time study was conducted for one formulation to validate the "click" feature of the thiol-ene reaction. Transmission mode was used having a SiC wafer as substrates for the spreading of the resin. A film-bar with a thickness of 12 μm was employed to coat the liquid formulation on the substrate. The UV-curing was performed by light emission of a Hamamatsu LIGHTINGCURE LC8 which was directed on the sample by an optic fiber.

Dynamic Scanning Calorimetry (DSC). A Mettler TOLEDO DSC-1 equipped with Gas Controller GC100 was employed to carry out the tests. Samples of about 5–10 mg were sealed in 40 μL aluminum pans and analyzed by DSC. The data were analyzed with Mettler Toledo STARe software V9.2. The following method was used to analyze the different thermosets. The starting temperature was set at room T; the first heating goes from 25 °C to 100 °C to eliminate the thermal history of the polymers; after that, the chamber was again cooled until −40 °C was reached and finally was a second heating from −40 °C to 250 °C applied. After each dynamic step, isothermal steps of 5 min were done to stabilize the chamber and the sample. The heating and the cooling rates were set at 10 °C/min and the analysis was performed in a controlled atmosphere with a N_2 flow rate of 40 mL/min. All the data were analyzed with Mettler Toledo STARe software V9.2.

Photo Dynamic Scanning Calorimetry (photo-DSC). Photo-DSC was used to monitor the photo-curing process in order to study the best condition. A Mettler TOLEDO DSC-1 equipped with Gas Controller GC100 was used to cure the liquid resins. A mercury lamp, Hamamatsu LIGHTINGCURE LC8, with an optic fiber was used to directly irradiate the samples. The emission of UV-light was centered at 365 nm. About 5–10 mg of photoc-

urable formulation was placed in an open aluminum pan (40 μL), whereas an empty pan was used as a reference. The tests were done at 25 °C and in a controlled atmosphere (N_2 flow of 40 mL/min). The scanning was performed with different steps: 2 minutes of stabilization of the sample, then a first irradiation of 5 min followed by 2 minutes of no light and 5 minutes again of UV-light to properly evaluate the UV-curing. The second run was done to confirm the complete curing and create the baseline. The integration of the final thermogram, retrieved from the subtraction of the two steps with UV on, gave the evolution of the heat of polymerization. From this data, it was possible to calculate the conversions as well as from the h_{peak} it was possible to have an indication about the rate of polymerization.

Photo-rheology & Viscosity. The UV-curing process was followed by means of photo-rheology analysis performed with an Anton Paar MC 302 rheometer (Physica MCR 302, Graz, Styria). The rheometer settings were the following: plate-plate geometry, the outside diameter of the upper metal disk was 25 mm, bottom support made of a quartz disk to guarantee the irradiation of the sample, distance between the plate was 200 μm which corresponds to 150 μL of the formulation. The UV-light was provided by a Hamamatsu LIGHTINGCURE LC8 and it was directed on the sample by means of an optic fiber. The lamp was turned on after 60 seconds of stabilization and the measurements were performed in oscillatory condition at a frequency of 1 Hz, with strain 1%. The tests were done in isothermal conditions at 25 °C.

The same instrument, Anton Paar MC 302 rheometer (Physica MCR 302, Graz, Styria), was also used for viscosity measurements. The geometry was set as plate-plate with both metal-based disk. The analysis was performed at room temperature with a distance between the plate of 200 um. The viscosity was measured by applying an increased shear stress from 0.01 to 1000 1/s.

Gel content. The gel content percentage (*% gel*) was evaluated on UV-cured samples. The UV-cured samples of about 100 mg were immersed in chloroform for 24 h at room temperature. The samples after the immersion were allowed to dry for 24 h in air to remove the trace of solvent. % gel was calculated by weight loss before and after the immersion in the solvent according to Equation 3.

$$\%\ gel = \frac{W_1}{W_0} \times 100 \tag{3}$$

where W_1 is the weight of the dry film after the treatment and W_0 is the weight of the dry sample before the treatment.

Dynamic mechanical thermal analysis (DMTA). A Triton Technology instrument was used to perform the dynamic-mechanical analysis of the UV-cured thermosets. The heating rate was 3 °C/min and the initial temperature of −40 °C was achieved by cooling down the test chamber with liquid nitrogen. A uniaxial tensile stress at a frequency of 1 Hz was applied on the sample. The T_g was detected as maximum of *Tan δ* curve and the analyses allowed the monitoring of the trend of the storage modulus in the temperature interval; the tests were stopped after the rubbery plateau. The samples were UV-cured in a silicon mold with an average dimension of 0.5 × 8 × 10 mm^3. Equation 4 is derived from the statistical theory of rubber elasticity and gives an estimation of the density of cross-links.

$$\nu_c = \frac{E'}{3RT} \tag{4}$$

where ν_c is the number of crosslinks per volume of the crosslinked network, E' is the storage modulus in the rubbery plateau ($T_g + 50$ °C), R is the gas constant and T is the temperature expressed in Kelvin.

Tensile & compression test. The mechanical properties of the thermoset were investigated by tensile and compression tests. The stress-strain curve was registered using a tensile instrument (MTS QTestTM/10 Elite, MTS System Corporation) combined with a measurement software (TestWorks® 4, MTS System Corporation). For the tensile test, a 1 KN load cell was used, and the traverse speed of the machine was set as 5 mm/min while for the compression test, a 25 KN load cell was employed, and the speed was 2 mm/min. Five samples were tested and the results reported are based on the average of three consistent measurements. The samples for the tensile test were 5B type dog bone in accordance with ISO527. ISO 527 is an international standard for determining the tensile properties of plastics, including thermosets. Instead, the samples for the compression test were cube of 10 × 10 × 4 mm^3 in accordance with ISO 604:2002. The Young's modulus was evaluated as the tangent of the curve up to the linear region (around 20% of total elongation), while the toughness (*U*) was evaluated as the area under the stress-strain curve. The result was the average value of at least 3 measurements.

3D scanning. The printed objects were scanned with a 3Shape E3 scanner to verify the precision and accuracy of the print. To achieve the best image acquisition, the samples were coated with magnesium stearate and then placed on the 3D scanner's platform. Lastly, a deviation analysis was performed providing the resulting scanned image and the original CAD to the CA Analyzer software which overlaps the two files comparing structure and dimensions.

Curing depth measurement. Jacob's curves were derived from the material testing performed on the DLP printer with a light intensity of 57 mW/cm^2 varying the exposure time. The resins were printed on the VAT without the platform at different exposure times, then the printed part was rinsed with solvent and the thickness was measured to evaluate the curing depth at a given exposure. Then Equation 1 (*vide supra*) was used to evaluate the minimum C_d and E_C.

Monomer Synthesis

*Synthesis of **HO-LGOL**.* In a 2 L round bottom flask, 10 g of LGO (79.39 mmol) wa diluted in 1 L Milli Q water (1M). 861 mg of K_3PO_4 (0.05 equivalent) were slowly added to the solution and allowed to stir for 5 h. After that time the base was neutralized

with 2.1 mL of 1M HCl, then the water was evaporated and the product (**HO-LGO**) was recovered as a yellow oil (82% yield) after column chromatography (Eluent: cyclohexane/ethyl acetate 80/20 to cyclohexane/ethyl acetate 45/55).

Then, in a round-bottom flask, 8.09 g of **HO-LGO** were dissolved in 225 mL of EtOH (0.25 M) and cooled down in an ice bath. 2.12 g of $NaBH_4$ (1.0 eq.) were added slowly to the reaction and allowed to stir for 5 minutes before the ice bath was removed. After 15 minutes, the starting material was consumed and the reaction was quenched with 5 mL acetone, then EtOH was evaporated and the crude was purified over column chromatography (Eluent: acetate/methanol 92/8) to get **HO-LGOL** (Figure S1) as a colourless oil (7.71 g, 94%).

^{1}H NMR (300 MHz, DMSO-d_6): δ 5.09 (s, 1H, H-1), 4.86 (d, J= 4.9 Hz, 1H, H-2), 4.74 (d, J=4.7 Hz, 1H, H-4), 4.27 (m, 1H, H-5), 3.66–3.52 (m, 4H, H-2′, H-4′, H-6, H-6), 1.68 (ddd, J=13.7, 6.2, 1.8 Hz, 1H, H-3), 1.57–1.47 (m, 1H, H-3).

^{13}C NMR (75 MHz, DMSO-d_6): δ 103.1 (C-1), 76.9 (C-5), 67.1 (C-4), 66.2 (C-2), 66.1 (C-6), 33.8 (C-3).

IR (cm^{-1}): 3350 (-OH); 2952; 2897; 1337; 1137; 1047; 967; 863; 781; 689.

$[\alpha]_D$: -3.26 (20.5 °C), 0.2 g/mL MeOH,

HRMS: $[M+Na]^+$ *m/z* calcd.: 169.0471. Exp.: 169.0473.

General procedure used for the synthesis of the different monomers. **HO-LGOL** (6 g) was weighed in a round-bottom flask. In the following order, 4Å molecular sieves, carboxylic acid (2.2 eq.) and DMAP (0.1 eq. with respect to the acid) were added. The mixture was then dissolved in 82 mL of DCM to achieve a final concentration of 0.5 M based on **HO-LGOL**. The solution was then cooled in an ice bath and flushed with N_2. Then DCC (0.1 eq; with respect to the acid) was slowly added to start the reaction. After a few minutes the ice bath was removed and N_2 flux was stopped. The mixture was allowed to stir for 1 h (the reaction completion was confirmed by TLC). Then the crude was filtrated through a celite pad and washed twice with a solution of 1M HCl and twice with saturated sodium bicarbonate. The crude was dried over anhydrous magnesium sulfate, filtered and concentrated. Finally, the desired product was then purified by column chromatography (Eluent: cyclohexane).

LGO-(O-But)$_2$ - LGO.M1 (83 % Yield) (Figure S2)

^{1}H NMR (300 MHz, $CDCl_3$): δ 5.98–5.82 (m, 2H, H-8, H-8′), 5.43 (s, 1H, H-1), 5.21–5.12 (m, 4H, H-9, H-9′), 4.98–4.93 (m, 1H, H-2), 4.86 (m, 1H, H-4), 4.58 (m, 1H, H-5), 3.85 (m, 2H, H-6), 3.16–3.08 (m, 4H, H-7, H-7′), 2.15–2.07 (m, 1H, H-3), 1.98–1.89 (m, 1H, H-3).

^{13}C NMR (75 MHz, $CDCl_3$): δ 171.1 (C=O), 170.8 (C=O), 129.7 (C-8, C-8′), 119.1–118.9 (C-9, C-9′), 100.2 (C-1), 74.3 (C-5), 69.8 (C-4), 69.1 (C-2), 66.1 (C-6), 39.0–38.9 (C-7, C-7′), 26.1 (C-3).

IR (cm^{-1}): 2973; 2897; 1684; 1470; 1289; 1220; 1115; 1101; 1046; 964; 905; 691.

$[\alpha]_D$: -2.62 (22.8 °C), 0.02 g/mL $CHCl_3$

HRMS: $[M+H]^+$ *m/z* calcd.: 283.1176. Exp.: 283.1170.

LGO-(O-Pent)$_2$ - LGO.M2 (93 % Yield) (Figure S3)

^{1}H NMR (300 MHz, $CDCl_3$): δ 5.89–5.73 (m, 2H, H-9, H-9′), 5.43 (s, 1H, H-1), 5.10–4.94 (m, 5H, H-2, H-10, H-10′), 4.86 (br s, 1H, H-4), 4.57 (m, 1H, H-5), 3.86 (m, 2H, H-6), 2.51–2.35 (m, 8H, H-7, H-7′, H-8, H-8′), 2.12–2.05 (m, 1H, H-3), 1.98–1.87 (m, 1H, H-3).

^{13}C NMR (75 MHz, $CDCl_3$) δ 172.5 (C=O), 172.3 (C=O), 136.3 (C-9, C-9′), 115.8–115.7 (C-10,C-10′), 100.3 (C-1), 74.4 (C-5), 69.5 (C-4), 68.8 (C-2), 66.6 (C-6), 33.5–33.4 (C-7,C-7′), 28.8 (C-8,C-8′), 27.5 (C-3).

IR (cm^{-1}): 3079; 2977; 1733; 1640; 1443; 1351; 1247; 1115; 1044; 986; 788; 667.

$[\alpha]_D$: -2.22 (23.0 °C), 0.02 g/mL $CHCl_3$

HRMS: $[M+H]^+$ *m/z* calcd.: 311.1489. Exp.: 311.1490.

Enzyme-Catalyzed Esterification

In a 10 mL round-bottom flask, **HO-LGOL** (approximately 4 mmol) and carboxylic acid (2.2 eq of 9-decenoic or 10-undecenoic acid) were mixed at 80 °C and 25 mbar in a Schlenk line and then CAL-B was added (10% w/w). The reaction was incubated overnight and the consumption of the starting material was confirmed by TLC. After that, the flask was cooled down, acetone (5 mL) was added and the mixture was stirred for 30 minutes. Finally, the enzyme was removed by filtration. The crude was subjected to chromatography (eluent: cyclohexane) to purify the desired products, obtained in 66% and 43%, respectively. The corresponding products, ^{1}H and ^{13}C NMR analyses are shown in Figure S4 and S5.

Formulation and Photocuring

The synthetized allyl ethers were tested for thiol-ene chemistry in synergy with a tetrafunctional commercial thiol (PETMP) which was used to make the formulations. The ratio between ene and thiol was kept 1:1 and the photoinitiator (PhI) was added to the mixture of monomers. The PhI, BAPO (1.5 % w/w), was added according to preliminary tests performed to find the optimal amount necessary to achieve high conversion. The resins were kept in brown vials to avoid light contact and they were mixed in an ultrasound bath for 5 minutes in order to disperse uniformly all components. Successively the formulations were cured in a silicon mold to create the specimens for DMTA, DSC, and tensile analysis. A Flood DMAX UV lamp was used as a UV-source. The emission spectrum of the UV-lamp was from 275 to 500 nm with a maximum located to 365 nm. The total dose of UV-light was 6000 mJ/cm^2.

3D Printing

The 3D printing DLP process was executed with an Asiga MAX X UV 27 DLP printer operating a 385 nm LED light source. CAD models of the different geometries were designed and exported to .stl files to be uploaded into the printer software Asiga

Composer. Light intensity was set to 40 mW/cm^2 and the layer thickness was 100 nm. The printing parameters were set according to the material test performed. After the 3D printing, samples were immersed in isopropanol and left for 10 minutes in an ultrasound bath to remove the unpolymerized formulations present on the surface. Subsequently, samples were subjected to UV-post curing performed in a Robot Factory UV-chamber equipped with a medium-pressure mercury lamp for 1 min.

Chemical Degradation

The chemical degradation was performed in an alkaline environment of NaOH 2M. The UV-cured samples of about 100 mg were immersed in the solution and weighed after a certain time. The weight loss was registered and followed according to Equation 5 to verify the degradability of the UV-cured thermoset.

$$Residual\ weight\ (\%) = \frac{W_t}{W_i} * 100 \quad (5)$$

where W_t is the weight of the dry film after the treatment in the alkaline environment for a specific time (t) and W_i is the weight of the UV-cured sample at the initial stage.

Acknowledgments

URD ABI acknowledges the Grand Reims, Grand Est Region and Conseil Départemental de la Marne for their financial support. This study was partially carried out within the Agritech National Research Center and received funding from the European Union Next-GenerationEU (PIANO NAZIONALE DI RIPRESA E RESILIENZA (PNRR) – MISSIONE 4 COMPONENTE 2, INVESTIMENTO 1.4 – D.D. 1032 17/06/2022, CN00000022). This manuscript reflects only the authors' views and opinions, neither the European Union nor the European Commission can be considered responsible for them.

Conflict of interests

The authors declare no conflict of interest.

Data Availability Statement

The data that support the findings of this study are available in the supplementary material of this article.

Keywords: UV-curing · thiol-ene · levoglucosenone · DLP 3D printing · bio-based

[1] M. Hong, E. Y.-X. Chen, *Trends Chem.* **2019**, *1*, 148–151.
[2] P. A. Owusu, S. Asumadu-Sarkodie, *Cogent Eng.* **2016**, *3*, 1167990.
[3] J. J. Bozell, G. R. Petersen, *Green Chem.* **2010**, *12*, 539–554.
[4] G. John, S. Nagarajan, P. K. Vemula, J. R. Silverman, C. K. S. Pillai, *Prog. Polym. Sci.* **2019**, *92*, 158–209.
[5] A. Gandini, *Macromolecules* **2008**, *41*, 9491–9504.
[6] M. V. Galkin, J. S. M. Samec, *ChemSusChem* **2016**, *9*, 1544–1558.
[7] I. Haq, P. Mazumder, A. S. Kalamdhad, *Bioresour. Technol.* **2020**, *312*, 123636.
[8] L. Pezzana, E. Malmström, M. Johansson, M. Sangermano, *Polymers* **2021**, *13* (9), 1530
[9] A. Gandini, T. M. Lacerda, *Prog. Polym. Sci.* **2015**, *48*, 1–39.
[10] G. Cazacu, M. Capraru, V. I. Popa, Advances Concerning Lignin Utilization in New Materials, *in Advances in Natural Polymers: Composites and Nanocomposites* (éd. Thomas, S., Visakh, P.M., et Mathew, Aji.P.), Springer, Berlin, Heidelberg, **2013**, p. 255–312.
[11] A. Etale, A. J. Onyianta, S. R. Turner, S. J. Eichhorn, *Chem. Rev.* **2023**, *123*, 2016–2048.
[12] J. G. Rosenboom, R. Langer, G. Traverso, *Nat. Rev. Mater.* **2022**, *7*, 117–137.
[13] M. S. Mettler, D. G. Vlachos, P. J. Dauenhauer, *Energy Environ. Sci.* **2012**, *5*, 7797–7809.
[14] G. R. Court, C. H. Lawrence, W. D. Raverty, A. J. Duncan, US Pat., 0 111 714. **2012**, *1*.
[15] S. Fadlallah, L. M. M. Mouterde, G. Garnier, K. Saito, F. Allais, Cellulose-Derived Levoglucosenone, a Great Versatile Chemical Platform for the Production of Renewable Monomers and Polymers. In *Sustainability & Green Polymer Chemistry Volume 2: Biocatalysis and Biobased Polymers*; ACS Symposium Series; American Chemical Society, 2020; Vol. 1373, pp. 5–77; ISBN 9780841298521.
[16] S. Fadlallah, A. A. M. Peru, L. Longé, F. Allais, *Polym. Chem.* **2020**, *11*, 7471–7475.
[17] C. M. Warne, S. Fadlallah, A. C. Whitwood, J. Sherwood, L. M. M. Mouterde, F. Allais, G. M. Guebitz, C. R. McElroy, A. Pellis, *Green Chem. Lett. Rev.* **2023**, *16*, 2154573.
[18] C. Herrlé, S. Fadlallah, S. Toumieux, A. Wadouachi, F. Allais, *Green Chem.* **2023**.
[19] A. Kayishaer, M. Annatelli, C. M. Hansom, L. M. M. Mouterde, A. A. M. Peru, F. Aricò, F. Allais, S. Fadlallah, *Macromol. Rapid Commun.* **2024**, *45*, 2300483.
[20] S. Fadlallah, A. Kayishaer, M. Annatelli, L. M. M. Mouterde, A. A. M. Peru, F. Aricò, F. Allais, *Green Chem.* **2022**, *24*, 2871–2881.
[21] S. Fadlallah, A. L. Flourat, L. M. M. Mouterde, M. Annatelli, A. A. M. Peru, A. Gallos, F. Aricò, F. Allais, *Macromol. Rapid Commun.* **2021**, *42*, 2100284.
[22] S. Fadlallah, P. Sinha Roy, G. Garnier, K. Saito, F. Allais, *Green Chem.* **2021**, *23*, 1495–1535.
[23] A. B. Scranton, C. N. Bowman, R. W. Peiffer, *Photopolymerization: fundamentals and applications*; ACS Publications, 1997; ISBN 0841235201.
[24] M. Sangermano, N. Razza, J. V. Crivello, *Macromol. Mater. Eng.* **2014**, *299*, 775–793.
[25] B. Lu, H. Lan, H. Liu, *Opto-electronics* **2018**, *1*, 170004.
[26] E. Sacco, S. K. Moon, *Int. J. Adv. Manuf. Technol.* **2019**, *105*, 4123–4146.
[27] M. Pagac, J. Hajnys, Q.-P. Ma, L. Jancar, J. Jansa, P. Stefek, J. Mesicek, *Polymer* **2021**, *13* (4), 598.
[28] V. S. D. Voet, J. Guit, K. Loos, *Macromol. Rapid Commun.* **2021**, *42*, 1–11.
[29] L. Pezzana, R. Wolff, G. Melilli, N. Guigo, N. Sbirrazzuoli, J. Stampfl, R. Liska, M. Sangermano, *Polymer* **2022**, *254*, 125097.
[30] L. Pezzana, R. Wolff, J. Stampfl, R. Liska, M. Sangermano, *Addit. Manuf.* **2024**, *79*, 103929.
[31] C. Noè, M. Hakkarainen, M. Sangermano, *Polymers (Basel).* **2021**, *13*, 1–16.
[32] R. Ding, Y. Du, R. B. Goncalves, L. F. Francis, T. M. Reineke, *Polym. Chem.* **2019**, *10*, 1067–1077.
[33] A. Cosola, R. Conti, H. Grützmacher, M. Sangermano, I. Roppolo, C. F. Pirri, A. Chiappone, *Macromol. Mater. Eng.* **2020**, *305*, 2000350.
[34] M. Claudino, J. M. Mathevet, M. Jonsson, M. Johansson, *Polym. Chem.* **2014**, *5*, 3245–3260.
[35] L. Pezzana, M. Mousa, E. Malmström, M. Johansson, M. Sangermano, *Prog. Org. Coat.* **2021**, *150*, 105986.
[36] L. Pezzana, G. Melilli, P. Delliere, D. Moraru, N. Guigo, N. Sbirrazzuoli, M. Sangermano, *Prog. Org. Coat.* **2022**, *173*, 107203.
[37] L. Pezzana, M. Sangermano, *Prog. Org. Coat.* **2021**, *157*, 106295.
[38] H. C. Kolb, M. G. Finn, K. B. Sharpless, *Angew. Chem. Int. Ed.* **2001**, *40*, 2004–2021.
[39] C. E. Hoyle, C. N. Bowman, *Angew. Chem. Int. Ed.* **2010**, *49*, 1540–1573.

[40] L. Breloy, C. A. Ouarabi, A. Brosseau, P. Dubot, V. Brezova, S. Abbad Andaloussi, J. P. Malval, D. L. Versace, *ACS Sustainable Chem. Eng.* **2019**, *7*, 19591–19604.
[41] A. C. Weems, K. R. Delle Chiaie, J. C. Worch, C. J. Stubbs, A. P. Dove, *Polym. Chem.* **2019**, *10*, 5959–5966.
[42] D. B. Larsen, R. Sønderbæk-Jørgensen, J. Ø. Duus, A. E. Daugaard, *Eur. Polym. J.* **2018**, *102*, 1–8.
[43] E. Çakmakçi, F. Şen, M. V. Kahraman, *ACS Sustainable Chem. Eng.* **2019**, *7*, 10605–10615.
[44] H. Şeker, E. Çakmakçi, *J. Polym. Sci.* **2020**, *58*, 1105–1114.
[45] M. K. Porwal, M. M. Hausladen, C. J. Ellison, T. M. Reineke, *Green Chem.* **2023**, *25*, 1488–1502.
[46] M. K. Stanfield, N. Kotlarewski, J. Smith, S. C. Thickett, *ACS Appl. Polym. Mater.* **2023**.
[47] A. L. Flourat, L. Pezzana, S. Belgacem, A. Dosso, M. Sangermano, S. Fadlallah, F. Allais, *Green Chem.* **2023**.
[48] N. B. Cramer, C. N. Bowman, *J. Polym. Sci. Part A* **2001**, *39*, 3311–3319.
[49] N. B. Cramer, J. P. Scott, C. N. Bowman, *Macromolecules* **2002**, *35*, 5361–5365.
[50] B. H. Northrop, R. N. Coffey, *J. Am. Chem. Soc.* **2012**, *134*, 13804–13817.
[51] E. Sanchez-Rexach, T. G. Johnston, C. Jehanno, H. Sardon, A. Nelson, *Chem. Mater.* **2020**, *32*, 7105–7119.
[52] C. Vazquez-Martel, L. Becker, W. V. Liebig, P. Elsner, E. Blasco, *ACS Sustainable Chem. Eng.* **2021**, *9*, 16840–16848.
[53] P. Esfandiari, S. C. Ligon, J. J. Lagref, R. Frantz, Z. Cherkaoui, R. Liska, *J. Polym. Sci. Part A* **2013**, *51*, 4261–4266.
[54] C. Resetco, B. Hendriks, N. Badi, F. Du Prez, *Mater. Horiz.* **2017**, *4*, 1041–1053.
[55] P. F. Jacobs, *Rapid prototyping & manufacturing: fundamentals of stereolithography*; Society of Manufacturing Engineers, 1992; ISBN 0872634256.

Manuscript received: March 22, 2024
Revised manuscript received: May 31, 2024
Accepted manuscript online: June 5, 2024
Version of record online: August 2, 2024